Boundary lubrication with a glassy interface

Anaël Lemaître[1,2] and Jean Carlson[1]
[1]*Department of Physics, University of California, Santa Barbara, California 93106, USA*
[2]*LMDH, Université Paris VI, UMR 7603, 4 place Jussieu case 86, 75005 Paris, France*
(Received 18 November 2003; revised manuscript received 16 March 2004; published 23 June 2004)

Recently introduced constitutive equations for the rheology of dense, disordered materials are investigated in the context of stick-slip experiments in boundary lubrication. The model is based on a generalization of the shear transformation zone (STZ) theory, in which plastic deformation is represented by a population of mesoscopic regions which may undergo nonaffine deformations in response to stress. The generalization we study phenomenologically incorporates the effects of aging and glassy relaxation. Under experimental conditions associated with typical transitions from stick-slip to steady sliding and stop-start tests, these effects can be dominant, although the full STZ description is necessary to account for more complex, chaotic transitions.

DOI: 10.1103/PhysRevE.69.061611 PACS number(s): 68.15.+e, 81.40.Pq, 46.35.+z, 46.55.+d

I. INTRODUCTION

Advances in developing nanometer scale technologies and devices are intrinsically coupled to fundamental progress in scientific understanding of the properties of materials under atomic scale confinement [1–34]. On one hand, friction, fracture, and plastic deformation at microscopic scales influence the operation and performance of engineered systems. On the other hand, investigation of clean, well characterized nanoscale systems is leading to additional insights into the underlying physical phenomena that govern systems under stress.

Increases in scientific computing capacity along with the development of experimental techniques have recently created opportunities for progress in both theory and measurements. The surface force apparatus (SFA) was originally designed to study solvation forces induced by a liquid confined between parallel surfaces [1,2]. Subsequently it was adapted to measure shear forces [3]. The SFA allows precise measurements on a microscopically thin layer of lubricant, separating atomically smooth (typically mica) surfaces. Friction and/or adhesion associated with a single asperity contact can be precisely measured. We focus here on friction and the associated stick-slip instabilities.

In many practical instances friction involves rough materials. However, for rough surfaces it can be difficult to identify the underlying mechanisms associated with complex phenomena (e.g., irregular dynamics and bifurcations). For rough materials individual asperity dynamics are *a priori* combined with any collective phenomena which may be associated with the population of contacts, and the population of contacts itself is necessarily time dependent. Rough surface measurements are thus naturally complementary to investigations of the plasticity and rheology of isolated, individual asperities. In addition, for single asperities, effects associated with interfacial materials (e.g., lubricants) are more easily isolated. Furthermore, there is growing evidence that the frictional properties of rough surfaces even at macroscopic scales are controlled by the plastic deformation of individual contacts [35]. Indeed, experiments have recently been designed that isolate and measure the dynamics of individual asperities at a rough dry interface, subject to shear [36].

In this paper we focus on the dynamics of an individual lubricated asperity contact. We model the lubricant using a set of constitutive equations which generalize the shear transformation zone (STZ) theory for amorphous, glassy materials. In addition to the STZ equations, the model incorporates the effects of glassy relaxation via the introduction of a state variable related to the internal free volume (the additional state variable may alternatively be thought of as an out-of-equilibrium effective temperature). The coupled STZ and free-volume dynamics were introduced previously and shown to capture a range of experimental phenomena in glassy and granular materials [37,38]. Here the constitutive equations model internal states of the lubricant. We perform a series of analytical and numerical calculations which mimic typical SFA experiments [15,29,31] and investigate the stationary states, the bifurcation diagram of the transition between stick-slip and steady sliding, the nature of this transition (i.e., super- or subcritical), the emergence of chaos, and aging of the yield stress in stop-start tests. At this stage, we primarily map out qualitative behaviors of the model. The compelling correspondence to existing experiments sets the stage for future, more detailed, quantitative comparison with data.

The remainder of this paper is organized as follows. Section II provides a brief overview of friction and boundary lubrication. Section III describes the free-volume constitutive equations and summarizes elements of STZ theory. Section IV contains the numerical and analytical results in scenarios representative of SFA experimental studies. Finally, we conclude in Sec. V with a discussion of our results, comparisons with experiments, and directions for continuing research.

II. BACKGROUND

In this section we provide a brief overview of boundary lubrication. Our emphasis is on unusual material properties and the associated modeling challenges which arise for atomically thin, confined liquid films. Note that, even for interfaces with relatively simple features, we still lack precise, quantitative, predictive models for friction. A more complete overview of recent results on friction and lubrica-

tion can be found in [12] and references therein.

In boundary lubrication a molecularly thin film of material is confined between two parallel surfaces. The relative motion of the surfaces is mediated by the plastic deformation of the interfacial material lubricating the contact. Molecularly thin films display specific properties which differ from the viscous behavior of bulk materials. Among the most noteworthy of these is the development of a yield stress for thin films at sufficiently low temperatures.

The changes of material properties under confinement can largely be attributed to a liquid-solid transition [5,7,8]. In some cases, numerical and experimental evidence suggests that layering occurs in the interfacial material [4–6,9,10,13,21,24] and the situation is similar to a liquid-crystal transition. That is, the material orders, and its deformation is expected to result from propagation of dislocations, or layer-over-layer sliding. In other cases, no evidence of ordering of the interfacial material is observed, and the liquid-solid transition induced by confinement enters the very large class of structural glass transitions [10,11,22,33]. In this case the material remains amorphous (liquidlike) but displays solidlike properties. The emergence of a yield stress is accompanied by power-law viscosities, as well as signs of glassy aging [29,31,36] and anomalous response spectra [22,25]. For some lubricants, either a glassy or layering transition can be observed, depending on features such as temperature [33], holding time, surface roughness [39], and commensurability of the surface and the film [24]. Consequences of solidlike ordering within the film include development of a static yield stress and stick-slip instabilities [14,15].

Boundary lubrication and the SFA experiments provide special opportunities for theory, because the interface is well characterized and precisely controlled, yet the system is large enough to display phenomena that also arise macroscopically. To date, models have primarily emphasized effects associated with ordering and interactions between the crystalline substrate and the lubricant. These aim to describe the effects of layering and surface induced order and involve (i) simple, reduced models of noninteracting particles in an effective periodic potential induced by the surfaces [23,26], (ii) Ginzburg-Landau functionals which account for heterogeneous ordering [19], or (iii) motion of adsorbate layers in the periodic potential associated with a regular surface [12,17,40].

Alternative approaches focus on internal properties of the lubricant, including contrasts between liquid- and solidlike properties and glassy behavior. Phenomenological rate and state friction laws have been introduced [20,27], in which the friction depends on the instantaneous slip rate and a state variable. The state variable models the collective dependence of friction on the internal degrees of freedom of the lubricant. This approach assumes the fluctuations are sufficiently self-averaging that microscopic degrees of freedom in the boundary layer can be ignored. This simplifying assumption was inspired by a large body of work in dry friction where rate-and-state formulations [41–44] have been shown to be useful to account for experimental data including stick-slip instabilities [45–49]. State variables can be motivated by experimental observations or molecular dynamics. For dry friction the state variable is related to the average lifetime of individual contacts, whereas in boundary lubrication the state variable is loosely connected to the degree of internal order in the lubricant. However, the friction laws these underlying mechanisms inspire are based more on macroscopic, thermodynamiclike criteria, than on the underlying microscopic physics at the interface.

Our model aims to provide a microscopically motivated description of the macroscopic forces which arise when the amorphous, interfacial lubricant is subject to shear. It relies on the assumption that the deformation of amorphous materials is controlled primarily by excluded volume effects, which dominate over fine details of molecular interactions. This is an old idea, advocated by Struik in the 1970s [50], and supported by striking similarities between very different amorphous systems. As a result, a relatively simple account of viscoplasticity is expected to hold for wide classes of amorphous systems. In the conclusion, we discuss how the equations we study here may account for the behavior of not only lubricants, but also sheared granular materials [51–54].

For the theorist, boundary lubrication has some special, simplifying features which in many respects make it an ideal template to study plasticity of amorphous materials. The interfacial lubricant layer is sufficiently thin that certain bulk phenomena, such as strain localization, appear to be avoided. As a consequence, boundary lubrication is, in fact, one of the few experimental setups where *homogeneous* constitutive equations can be directly tested. In contrast, for glassy bulk materials deformation organizes in shear bands, usually a few particle diameters thick, and the strain rate measured in an experiment is averaged over a nonuniform field. The origin of strain localization is poorly understood, but clearly a more complete understanding of simple homogeneous flows must be established first. No shear banding is expected to occur in nanoconfined films because the deformation is already confined at scales equal to or smaller than that which would be expected for the shear band. The SFA experimental setup closely resembles the sheared strip used in recent numerical studies of relaxation in glasses [30,32].

There are, however, several persistent challenges associated with the SFA. First, an astonishingly wide range of phenomena have been observed in this system for different lubricants under different conditions. The range of behaviors remains a puzzle which is difficult to piece together in the absence of a systematic theory that clearly captures the most basic observations. The variability of experimental observations might be attributed to inherent difficulties in the preparation of samples of any glassy material, due to the effects of aging. Certainly, capturing the full spectrum of properties is a long term target for theoretical models. Second, it is difficult to increase the stiffness of the apparatus beyond $\sim 3500\ \mathrm{N/m}$ [55]. A salient feature of boundary lubrication, which directly results from this finite stiffness, is the emergence of stick-slip instabilities at low velocity [5,7,14,15,29,31,33,56]. In the most dramatic cases, the transition to stick-slip is accompanied by irregular or chaotic behavior [7,31]. The main consequence of the stick-slip instability (and of the finite scanning length of the experimental apparatus), is that the SFA can provide stationary data only for limited ranges of strain rates. Thus for a wide range

of parameters information about the interfacial material can be gathered only through the observation of instabilities and transient dynamics. Therefore, it is essential to treat this finite stiffness explicitly in any theoretical approach. Ultimately, rather than hampering our understanding of structural glasses, stick-slip instabilities and transient dynamics provide us with much richer data than simple stationary states. These instabilities may help clarify important, general issues associated with the out-of-equilibrium properties of structural glasses.

The model we study in this paper is an intermediate statistical theory recently proposed [37,38,57] for sheared structural glasses. Here "intermediate" refers to the fact that our model falls between the thermodynamiclike, phenomenological rate and state descriptions which have been proposed for friction at dry and lubricated interfaces, and an atomistic statistical mechanical description of the lubricant, which takes into account detailed microscopic, molecular interactions. The model begins with shear transformation zone theory [58,59], which was inspired by molecular dynamics simulations of fracture in amorphous materials, and which provides a microstructural description of shear-induced rearrangements [58–60]. STZ theory accounts for the emergence of a yield stress in amorphous materials through introduction of state variables characterizing the anisotropy of structural arrangements. Drawing on earlier approaches to describing creep in metallic alloys [61–65], STZ theory models local shear rearrangements as activated processes, controlled by local density fluctuations. This leads to the introduction of free-volume activation factors, in the spirit of early theories of the glass transition [66–70].

In [37] and subsequent works [38], it was noted that previous approaches treat free-volume as a fixed parameter, although it clearly varies as the material dilates or contracts. In granular materials, for example, density relaxations have been observed and precisely characterized experimentally [71], inspiring several models of slow relaxation [71–73]. Dilatancy in granular material is also involved in the definition of frictional properties and stick-slip transitions [74]. Slow relaxation of volume or enthalpy is a ubiquitous feature accompanying the glass transition [50]. We expect more explicit modeling of the time dependence of density fluctuations may capture the emergence of a wide range of glassy properties near a jamming transition. The constitutive equations introduced in [37] were thus developed to address the question: How much glassy phenomenology can be captured by the simplest account of free-volume dynamics, coupled to the dynamics of shear transformation zones?

Previously it was shown that free-volume dynamics suffices to characterize aging and power-law rheologies, while the dynamics of shear transformation zones are required to account for the emergence of a yield stress [37,38]. In transient regimes, both processes may interact and contribute to rheological properties. Furthermore, chaotic behavior has been observed in the SFA close to the stick-slip instability [31], and it is known in overdamped frictional equations that two or more state variables are necessary to understand the occurrence of chaos. Here, we did not invoke an *ad hoc* theory with multiple state variables [75], but were led to it by the underlying physical mechanisms already associated with other, relevant experimental observations. Moreover, as chaos is difficult to characterize experimentally, significant insight is provided when observations are supplemented with theoretical models, to guide measurements and analysis.

Finally, we note that it is not *a priori* necessary to identify the additional state variable as a free volume. It was previously noted by Falk and Langer that free volume is related to the notion of Edwards' temperature [58,76–78]. As noted later [37,38], the essential feature that free-volume dynamics captures is the existence of an intensive quantity that measures internal disorder and evolves as the system orders or is driven away from equilibrium. Alternative approaches characterize the internal state in terms of an effective temperature [57]. Note, finally, that the concept of Edwards' temperature is likely to be related to effective temperatures arising in weak versions of the fluctuation-dissipation theorem [79–82]. In this paper, we use free-volume terminology and refer the reader to [57] where the relation between free volume and effective temperature is discussed in more detail.

III. CONSTITUTIVE EQUATIONS

Our presentation of the model is broken down into four steps: (i) preliminaries associated with the SFA, explicitly accounting for the finite stiffness, (ii) STZ theory, (iii) the free volume equations, and (iv) rescaling to obtain dimensionless equations. The equations in Secs. III B–III D have been presented elsewhere, but we include their derivation for the sake of completeness. We refer the reader to [58] and [37,38,57] for more detailed discussions of the underlying assumptions.

A. Surface force apparatus

A primitive model of the SFA consists of a single slider block, pulled along a surface by a spring of stiffness k. The opposite end of the spring advances at a prescribed velocity V. Letting x denote the displacement of the block relative to the stationary surface, the spring exerts a force $F=k(Vt-x)$, where t is time measured from some initial time $t=0$ when $x=0$. The block is subject to both the pulling force from the spring and frictional resistance at the surface. Modeling the SFA as a single slider assumes that the sliding surface is sufficiently small, rigid, and uniform and that friction at the contact is sufficiently self-averaging that slip occurs uniformly across the interface.

Assuming the thickness h of the interface remains constant, the motion of the slider is related to the rate of shear deformation $\dot{\gamma}$ of the interfacial material by $\dot{x}=2h\dot{\gamma}$. If the area S of the contact is constant, the shear stress exerted by the slider on the interfacial material can be written as $\sigma=F/S$. Furthermore, for the experiments we consider, the friction is sufficiently strong that the motion is overdamped, and inertial forces associated with the nonzero mass of the slider can be neglected. This leads to an equation of motion for the stress:

$$\dot{\sigma}=\mu(\dot{\epsilon}-\dot{\gamma}) \tag{1}$$

with $\mu=hk/S$ and $\dot{\epsilon}=V/(2h)$. The motion $\dot{x}(t)$ of the slider follows from the solution to Eq. (1), which depends on how

the strain rate $\dot{\gamma}$ is related to the shear stress σ and the internal state variables.

We next define the constitutive equations which couple the free-volume and STZ dynamics. Later we restrict our discussion to subsets and (linearized) simplifications of these equations to isolate effects associated with distinct state variables and/or nonlinearities, and to illustrate phenomena that require a larger number of state variables to be resolved.

B. Elements of STZ theory

STZ theory is based on the idea that the macroscopic deformation of an amorphous material results from localized rearrangements involving cooperative molecular motion at mesoscopic scales [83–85]. The loci of such rearrangements are called shear transformation zones, and the internal state of the system is characterized by their number density. In its simplest form, STZ theory involves only two types of zones (labeled "+" and "−," with number density n_+ and n_-, respectively) oriented along the principal axes of the shear stress. Zones of each type transform into one another during an elementary shear. The average strain rate $\dot{\gamma}$ is given by

$$\dot{\gamma} = \mathcal{A}_0(R_+ n_+ - R_- n_-). \tag{2}$$

Here $\dot{\gamma}$ is averaged over the populations of zones, $n_\pm$, that reorient with probabilities $R_\pm$, respectively.

The important insight Falk and Langer contributed to previous STZ theories was to treat the populations densities $n_\pm$ as state variables and propose equations of motion for the populations. These take the following form [58,59]:

$$\dot{n}_\pm = - R_\mp n_\mp + R_\pm n_\pm + \sigma\dot{\gamma}(\mathcal{A}_c - \mathcal{A}_a n_\pm). \tag{3}$$

The first two terms on the right hand side account for exchanges between the populations of STZ's due to mesoscopic rearrangements, while the last term introduces a coupling with the mean flow, through creation of STZ's at rate $\mathcal{A}_c$ and annihilation at rate $\mathcal{A}_a$. The equations describe how shear deformations induce small displacements of the molecules, hence creating and destroying shear transformation zones. In this framework, the emergence of a yield stress in amorphous solids at low temperature is associated with the mobilization of zones when stress is applied.

C. Free-volume activation

In the original formulation of STZ theory, the rates were estimated to be nonlinear functions of stress. Derivation of the rates were based on free-volume activation, as developed by Cohen, Turnbull, and co-workers to understand the phenomenology of the glass transition [68–70]. Specifically, the rates $R_\pm$ were estimated to be of the form $\exp[-v_0(\pm\sigma)/v_f]$, where v_0 is a stress-dependent activation volume, and v_f is a material-dependent constant. The detailed formulation of transformation rates $R_\pm$ is not essential to capture the STZ mechanism for jamming. Instead, a first order approximation for the stress dependence of the rates $R_\pm$ is sufficient [58,59].

However, for hard-sphere systems, the free volume v_f is directly related to the density. There is no reason to believe that it should take a fixed value as a function of pressure and temperature. On the contrary, it is a dynamical quantity which evolves as the material dilates or contracts. This observation naturally leads to dynamical equations for the free volume, written in analogy with the equations of motion for the populations $n_\pm$ [37,38].

The activation factors depend on both free-volume and stress fluctuations. Assuming these effects are uncorrelated, we express the rates as

$$R_\pm(\sigma, v_f) = R_0 \exp\left[-\frac{v_0}{v_f}\right]\exp\left[\pm\frac{\sigma}{\overline{\mu}}\right]. \tag{4}$$

An elementary shear rearrangement takes a "+" oriented zone to a "−" oriented zone, or vice versa, and occurs if sufficient free volume (large than v_0) is available, and if the virtual work of shear forces promotes the transition in the $\pm \to \mp$ direction. The variable $\overline{\mu}$ is here a scale of forces (not to be confused with the elastic modulus μ) which may depend on temperature, and governs stress activation factors. Note that the introduction of backward and forward jumps is an old idea, already present in Eyring's theory of viscous liquids [86] or in Spaepen's approach to creep in metallic glasses [61].

The equation of motion for v_f is given by [37,38]

$$\dot{v}_f = - R_1 \exp\left[-\frac{v_1}{v_f}\right] + \mathcal{A}_v \sigma\dot{\gamma}. \tag{5}$$

Here the free-volume dynamics involve two competing mechanisms: (i) activated elementary compaction which increases the density, and (ii) the transfer of macroscopic work into enthalpy, which dilates the material. The parameter $\mathcal{A}_v$ specifies how efficiently the work of external forces is used in dilatancy. The parameter R_1 is an update frequency, which should be of the same order as R_0; the activation volume v_1 may differ from v_0, because the two elementary rearrangements (shear and compaction) involve different relative motion of the molecules and hence different reactional pathways. The ratio $\kappa = v_1/v_0$ is an essential parameter of the theory and is expected to depend on the shape of the molecules.

The equations described here correspond to the low temperature limit of a more general set of equations for the dynamics of a disorder temperature [57]. We will restrict our current discussion to this free-volume formulation. As we will show, it captures a wide range of phenomena observed experimentally.

D. Rescaling and change of variables

For the constitutive equations defined above [Eqs. (2), (3), and (5)], it is convenient to introduce reduced variables [58,59]

$$\Delta = \frac{n_- - n_+}{n_\infty}, \quad \Lambda = \frac{n_- + n_+}{n_\infty}, \quad \text{and} \quad \chi = \frac{v_f}{v_0}, \tag{6}$$

along with the rescaled parameters $n_\infty = 2\mathcal{A}_c/\mathcal{A}_a$, $\epsilon_0 = \mathcal{A}_0\mathcal{A}_c/\mathcal{A}_a$, $\mu_0 = 1/(\mathcal{A}_0\mathcal{A}_c)$, $E_0 = 2\epsilon_0 R_0$, and $E_1 = R_1/v_0$. This change of variables leads to the following set of equations:

$$\dot{\gamma} = E_0 \exp\left[-\frac{1}{\chi}\right]\left[\Lambda \sinh\left(\frac{\sigma}{\bar{\mu}}\right) - \Delta \cosh\left(\frac{\sigma}{\bar{\mu}}\right)\right], \quad (7)$$

$$\dot{\Delta} = \frac{\dot{\gamma}}{\epsilon_0}\left(1 - \frac{\sigma}{\mu_0}\Delta\right), \quad (8)$$

$$\dot{\Lambda} = \frac{\sigma\dot{\gamma}}{\mu_0\epsilon_0}(1-\Lambda), \quad (9)$$

$$\dot{\chi} = -E_1 \exp\left[-\frac{\kappa}{\chi}\right] + \alpha\sigma\dot{\gamma}. \quad (10)$$

Equations (7)–(9)—the free volume χ in Eq. (10) being held constant—are almost identical to the original formulation of STZ theory by Falk and Langer [58,59]. The variable Λ accounts for the total density of STZ's. The steady state value $\Lambda=1$ is a stable fixed point. In STZ theory, Λ differs from 1 only in the initial transient, and its initial value is expected to depend on the type of annealing performed during the creation of a glass from a high temperature liquid. Here we are not concerned with transient features associated with these annealing-dependent initial values of Λ and will assume $\Lambda=1$ throughout. This eliminates Eq. (9). The variable Δ is the normalized difference between "+" and "−" STZ densities. It accounts for the anisotropy of the molecular structure. For a fixed applied stress σ (and fixed free volume χ), Eqs. (7) and (8) were shown previously to account for a transition between an elastic regime (jamming) and a viscoplastic regime (flowing). The transition occurs at a yield stress σ_y satisfying

$$\tanh\left(\frac{\sigma_y}{\bar{\mu}}\right) = \frac{\mu_0}{\sigma_y}. \quad (11)$$

The variable χ is a normalized free volume, which accounts for the existence of disorder in the molecular structure. Its dynamics, determined by Eq. (10), couples with Eqs. (7) and (8) only as long as χ appears in the prefactor of Eq. (7), setting the time scale of elementary shear events.

At a fixed applied stress σ, Eqs. (7), (8), and (10) account for plastic deformation resulting from the coupled dynamics of Δ and χ. When the system is driven at a constant shear rate as in the SFA, these equations must be supplemented with Eq. (1), which accounts for coupling of the material deformation with a compliant driving apparatus.

E. Discussion

Most of the results presented here are consequences of the free volume dynamics (10) coupled to Eq. (7), the STZ variables Δ (and Λ) being held constant ($\Delta=0$ and $\Lambda=1$). In this case, Eqs. (7) and (10) reduce to

$$\dot{\gamma} = E_0 \exp\left[-\frac{1}{\chi}\right]\sinh\left[\frac{\sigma}{\bar{\mu}}\right], \quad (12)$$

$$\dot{\chi} = -E_1 \exp\left[-\frac{\kappa}{\chi}\right] + \alpha\sigma\dot{\gamma}. \quad (13)$$

These equations can also be linearized for small stresses, which enables us to eliminate the parameter $\bar{\mu}$ (taken to unity) which enters the exponential activation factors to fix a scale of stresses. The linearized (in σ) equations are

$$\dot{\gamma} = E_0 \exp\left[-\frac{1}{\chi}\right]\sigma, \quad (14)$$

$$\dot{\chi} = -E_1 \exp\left[-\frac{\kappa}{\chi}\right] + \alpha\sigma\dot{\gamma}. \quad (15)$$

We refer to this as the *stress-linear* approximation. It captures most of the phenomenology accompanying the stick-slip instability and allows for interesting analytical calculations.

Throughout this paper, we will use these three sets of equations—the full, coupled system of equations including STZ and free-volume effects, the nonlinear equations describing free-volume dynamics only, and the linearized version of the free-volume equations—in order to clarify the consequences of our assumptions and the role of the different state variables. The questions raised are as follows. What behavior is already captured by free-volume dynamics, in the stress-linear version [Eqs. (14) and (15)]? What is the importance of the activation factors and the nonlinear dependence of strain rate versus stress [Eqs. (12) and (13)]? What are the expected consequences of the interaction between several internal state variables, as modeled by Eqs. (7), (8), and (10)?

IV. COMPARISON WITH EXPERIMENTS

In this section we compare the qualitative behavior of our model with several important experimental protocols which are widely used to characterize the behavior of frictional interfaces. Two classes of experiments are especially relevant for our study.

(i) Boundary lubrication experiments involving confined fluids in a SFA. Here the geometry of the lubricated contact is well controlled but at the cost of limited shearing distance, which results in a limited range of accessible shear rates. Many interfacial materials have been studied in this setup, including spherical, linear, branched, and globular molecules. As discussed in Sec. II, two different types of behavior can be identified depending on the ordering properties of the material. Spherical molecules tend to order more easily, while branched molecules are more likely to enter a glassy regime [15]. Layer-over-layer sliding, in which molecules retain an ordered structure during shear, is limited to very carefully controlled samples of spherical molecules. More often, packing and confinement of irregularly shaped molecules and/or the shearing motion induces disorder and glassy behavior. Experimental observations indicate that materials which are glassy under confinement present a set of similar properties, which are the focus of our study.

(ii) Asperity friction involving nominally dry, rough, surfaces [36]. In this case, the contact between two surfaces is

composed of a sparse set of load bearing asperities. In general, the frictional response of dry surfaces results from the dynamics of creation and destruction of these asperities [44,87], but an experimental protocol has been designed by Bureau *et al.* which uses dry friction measurements to access an entirely different physics [36]. It relies on the property that the stress response of individual asperities involves plastic deformation of nanometer thick joints [35]. By performing studies at time scales for which the micro-contacts retain their identity [36], dry friction measurements thus grant access to the average rheology of an ensemble of plastic joints between load-bearing asperities. Because they probe the plasticity of the material, our STZ based theory is of direct relevance. Furthermore, according to Bureau *et al.* such measurements allow for a much larger shearing distance—while maintaining asperities at contact—and hence higher velocities than the SFA. However, they provide little control on the micrometric structure of individual asperities. The experiments of Bureau *et al.* were performed using PMMA [36], but contacts between many solids are expected to exhibit such disordered frictional joints. This is expected to be the case not only for solids which are disordered in the bulk, but also for most ordered solids, due to nanometric surface roughness, defects in the bulk, atomic surface misorientations, and/or the presence of adsorbates.

Both the SFA and the response of dry friction contacts involve plastic deformation of a molecular interface of thickness of order 1 nm and width of order 1 μm. The SFA allows independent measurement of normal and friction forces at the interface. Friction forces are found to scale with the external load [33], in agreement with Amonton's law, and forces are measured in units of millinewtons. The corresponding stress on a surface of area 1 μm^2 is of order 10^6 N/m^2, defining the typical unit of stress considered in our study. In contrast, dry friction measurements provide only indirect access to the normal load exerted on individual asperities. The friction force scales linearly with the stress, which is thought to arise from the increasing number of asperities with increasing load, whereas the typical value of the load exerted on any single asperity is expected to remain approximately constant, of the order of the yield stress of the bulk material [87].

Accessible driving velocities with the SFA range between 10^{-3} and 10 μm s^{-1}, while velocities studied in dry friction experiments range between 10^{-1} and 10^3 μm s^{-1}. Given the nanometer thickness of the molecular joints, velocities of order 1 μm s^{-1} translate into shear rates of order 10^3 s^{-1}. Time scales enter our equations through different constants. For example, for fixed $\dot{\epsilon}$ and E_0, a global rescaling of μ, E_1, and α changes the overall scale of the resulting dynamics. E_1 and E_0 both involve the update frequencies R_1 and R_0, which should be of the same order, but contain factors of rather different origins, and may present different dependencies on external pressure and temperature. In this present work, we will avoid speculative discussions about the specific values of these constants and their microscopic origin. We thus take constants of order 1 to develop a qualitative picture of the behavior emerging from our equations, and expect that a simple rescaling of these constants will permit us to bring our equation into rough quantitative agreement with experiments.

Most of our investigation focuses on the equations governing free-volume dynamics, either in their nonlinear form (12) and (13) or in their linear form (14) and (15). We study (i) stress versus strain rate relations in steady sliding, (ii) the transient dynamics upon start-up, and (iii) the transitions to stick-slip at low velocities. In the last part of our work, we focus on the existence of (iv) chaotic regimes of stick-slip. In order to observe chaos, we need the full (three-dimensional) set of nonlinear equations (7)–(10).

A. Steady sliding

The first step in characterizing the behavior of sheared materials is, of course, the steady state relation between stress and strain rate. In boundary lubrication and dry friction measurements, it has been observed that, at low velocities, the friction force is weakly velocity weakening. Velocity strengthening behavior at higher velocity is observed in dry friction measurements but typically not with the SFA. Of course, it is difficult to draw definite conclusions for fast driving rates due to the limited range of accessible velocities.

Below we calculate the stress vs strain rate relationship in order of increasing model complexity, beginning with the linearized free-volume equations, followed by the nonlinear free-volume equations, and finally for the complete model, including STZ's.

1. Stress-linear equations

In the stress-linear version of our model [Eqs. (14) and (15)] the ratio between stress and strain rate determines a viscosity

$$\eta = \exp(1/\chi)/E_0, \tag{16}$$

which is a simple function of the free volume χ.

Initially, we take the limit of infinite stiffness for the experimental apparatus, so that, from Eq. (1), $\dot{\gamma}=\dot{\epsilon}$. From Eqs. (14) and (15), the dynamics of χ reduces to

$$\dot{\chi} = -E_1 \exp\left[-\frac{\kappa}{\chi}\right] + \frac{\alpha}{E_0}\exp\left[\frac{1}{\chi}\right]\dot{\epsilon}^2. \tag{17}$$

The quantity χ admits a steady state value only if the shear rate is not too large. For high shear rates,

$$\dot{\epsilon} > \dot{\epsilon}* = \sqrt{\frac{E_0 E_1}{\alpha}}, \tag{18}$$

this equation becomes unstable, $\dot{\chi}$ is positive at all times, and χ diverges. This instability is not related to stick-slip, since it occurs for any value of the stiffness. It indicates that, at large shear rates, the material cannot dissipate the work of external forces and is driven toward a highly disordered state. Situations when $\dot{\epsilon} > \dot{\epsilon}*$ are by definition transient: the material does not reach a steady state. Instead χ diverges.

Interpreting χ as a free volume, this divergence may correspond to an opening of the interface, and possible loss of contact between the surfaces. In typical experiments, if such high shear rates were applied, the divergence of χ would be *a priori* limited by the scanning length of the experimental device. The divergence of χ is accompanied by an apparently

viscous behavior, with viscosity $\eta=\exp(1/\chi)/E_0\sim 1/E_0$ approximately independent of χ. It may appear, from a measurement of stress alone, that the system is stationary although the internal dynamics may not have reached a steady state.

The existence of this divergence at a critical driving shear rate $\dot{\epsilon}*$ arises physically from the fact that the transition probabilities are bounded. The factor $\exp(1/\chi)$ approaches unity at high χ, and becomes decreasingly sensitive to changes in the intensive variable χ when χ is much larger than 1. At this point, the free-volume dynamics is only weakly coupled to the other equations. Of course, if a high shear rate $\dot{\epsilon}>\dot{\epsilon}*$ is applied steadily, this divergence ultimately leads (in the $t\to\infty$ limit) the system toward a highly disordered, "fluidized," state. Our equations are not designed to describe this limit, and instead should start to break down when χ reaches some large value, say, χ_f. We expect $\chi_f\gg 1$ (here the value 1 corresponds to the activation free volume for an elementary shear transformation, which is much less than one molecular volume per molecule, whereas χ_f is of the order of one additional molecular volume of free space per molecule). We do not attempt to account for the late stages of this divergence, and only changes of material behavior around $\chi\sim 1$ are of interest to us. For this reason, and to simplify the discussion, we can safely take χ_f to infinity.

We could avoid explicit reference to such a divergence as several mechanisms could be invoked to explain the saturation of free volume at high velocity resulting in the emergence of another fixed point. Possible mechanisms include the weak density dependencies of various parameters, like E_0, E_1, or α, or higher order terms in the free-volume dynamics [Eqs. (10), (13), and (15)]. Here we study free-volume dynamics in the simplest form for several reasons. First, several mechanisms could be invoked to account for the saturation of free volume at high velocity, and it is unclear at this stage which would be dominant. Thus we prefer not to differentiate between them. Second, regardless of the mechanism, the approach to any high free-volume fixed point would, in its early stages, closely resemble the divergence we discuss here. Given the limited span of experiments, we expect that our model is relevant to observations that are currently available.

For shear rates smaller than $\dot{\epsilon}*$, the free volume admits a steady state value, and this leads to a relation between stress and strain rate, of the form

$$\sigma=\frac{\dot{\epsilon}^{\,n}}{E_0}\left(\frac{\alpha}{E_0E_1}\right)^{(n-1)/2}. \tag{19}$$

The constitutive equations thus account for power-law viscosity, with an exponent

$$n=\frac{\kappa-1}{\kappa+1} \tag{20}$$

which is directly related to the ratio $\kappa=v_1/v_0$ of activation volumes. For $\kappa>1$ the stress is an increasing function of the shear rate, the material is shear thickening. For $\kappa<1$, the stress is a decreasing function of the shear rate, the material is shear thinning. We will see that, in the latter case, the system exhibits a transition to stick-slip at low velocities.

2. Nonlinear free-volume equations

Next we calculate the stress vs strain rate for the nonlinear free volume equations (12) and (13). In this case, we obtain a generalization of Eq. (19) which is valid beyond the range of small stresses, where the linear-stress approximation is expected to hold. The resulting relationship is given by

$$\dot{\epsilon}=E_0\left(\frac{\alpha E_0}{E_1}\right)^{1/(\kappa-1)}\sigma^{1/(\kappa-1)}\left[\sinh\left(\frac{\sigma}{\bar{\mu}}\right)\right]^{\kappa/(\kappa-1)}. \tag{21}$$

For small σ, linearization of the hyperbolic sine leads to the power-law rheology described above [Eqs. (19) and (20)]. For large stresses, the right hand side is dominated by the exponential growth in the hyperbolic sine, which results in a logarithmic dependence of the stress σ on the strain rate $\dot{\epsilon}$.

As in the linearized case, Eq. (21) is accompanied by a condition imposed on the strain rate $\dot{\epsilon}$ which must be satisfied for there to be a self-consistent, steady state value of χ. Violation of the condition ($\dot{\epsilon}>\dot{\epsilon}*$) is associated with diverging free-volume and fluidization. For the nonlinear free-volume equations the constraint is more complicated than in the linearized case and is described by $\dot{\epsilon}/[E_0\sinh(\sigma/\bar{\mu})]=\exp(-1/\chi)<1$. A stationary value of χ exists if and only if the inequality is satisfied. Equivalently, a solution exists if and only if

$$\left[\frac{\alpha E_0}{E_1}\sigma\sinh\left(\frac{\sigma}{\bar{\mu}}\right)\right]^{1/(\kappa-1)}<1. \tag{22}$$

The case of equality in Eq. (22) can be used to define a critical value $\sigma*$:

$$\frac{\alpha E_0}{E_1}\sigma*\,\sinh\left(\frac{\sigma*}{\bar{\mu}}\right)=1. \tag{23}$$

Then, the validity of Eq. (22) depends on the value of σ relative to $\sigma*$. If $\kappa<1$, σ is a decreasing function of $\dot{\epsilon}$, and the condition (22) is met for $\sigma>\sigma*$, or equivalently $\dot{\epsilon}<\dot{\epsilon}*=\dot{\epsilon}(\sigma*)$. If $\kappa>1$, σ is an increasing function of $\dot{\epsilon}$, and the condition (22) is met for $\sigma<\sigma*$, or $\dot{\epsilon}<\dot{\epsilon}*$. In both cases, as with the linear equations, there is a limiting driving strain rate $\dot{\epsilon}*$ above which the material fluidizes, and (in our model) the high velocity fixed point is sent to infinity. For $\dot{\epsilon}>\dot{\epsilon}*$, as the quantity χ diverges, the relation between stress and strain rate reduces to

$$\dot{\epsilon}=E_0\sinh\left(\frac{\sigma}{\bar{\mu}}\right). \tag{24}$$

Stress appears to be increasing for large values of the strain rate.

These logarithmic relations between stress and strain rate are consistent with experimental observations. Specifically, with the SFA, the stress has been observed to be a decreasing function of the strain [29,33], consistent with a value of the parameter $\kappa<1$. This is based on steady state measurements covering more than two decades of the rescaled strain rate. The window of observation for these measurements was lim-

ited by the range of accessible driving velocities of the experimental apparatus at high shear rates, and by the emergence of stick-slip at low shear rates [29,33]. No stress increasing branch is observed at higher shear rate (this could be due to these experimental limitations). Gourdon and Israelachvili have measured frictional response of the SFA at different normal loads [33] and shown that Amonton's law is satisfied: the friction force is proportional to the normal force. In the framework of our model, this is consistent with the assumption that the parameter $\bar{\mu}$ is proportional to the normal stress: $\bar{\mu}=\bar{\alpha}p$. From measurements of the reduced slope by Gourdon and Israelachvili [33] and Eq. (21) we estimate $\bar{\alpha}(\kappa-1)/\kappa \sim -6\times 10^{-2}$.

In comparison, dry friction measurements of joint plasticity provide a rather different picture. A decreasing branch of the stress–strain–rate relation is observed on a small interval of lower velocities, up to a limit driving velocity of order 1 μm s^{-1}. Above this velocity, stress increases logarithmically over two decades in the scaled strain rate. There are two different ways to interpret these data in the framework of our model.

(i) The increasing branch corresponds to the true steady state expression (21) for $\epsilon<\epsilon^*$ and $\kappa>1$, and our model does not capture the decreasing part.

(ii) The velocity at which the stress starts to increase with increasing strain rate corresponds to $\dot{\epsilon}^*$. In this case, the stress decreasing branch should be fitted with Eq. (21) for $\kappa<1$, but the limited range of experimental data does not provide an accurate estimate of the prefactor in this expression. The logarithmic stress increase allows us to estimate a constant in the expression (24).

In either case, the stress increasing branch in experimental data can be used to extract information about Eq. (21) or Eq. (24). The slope of σ vs $\log_{10}\dot{\epsilon}$ in these equations is $(\kappa-1)\bar{\mu}/\kappa$ and $\bar{\mu}$, respectively. The measured value for this prefactor is $5\times 10^{-2}\sigma_0$ [36], where σ_0 is a reference stress, of the order of the load $\bar{p}$ sustained by individual joints, which is of the order of the yield stress of the bulk material [87].

3. Full free-volume and STZ equations

Finally, we explore the steady state stress vs strain rate relationship using the complete set of equations (7)–(10). In this case, the steady state relation between stress and strain rate reads

$$\dot{\epsilon}=E_0\left(\frac{\alpha E_0\sigma}{E_1}\right)^{1/(\kappa-1)}\left[\sinh\left(\frac{\sigma}{\bar{\mu}}\right)-\frac{\mu_0}{\sigma}\cosh\left(\frac{\sigma}{\bar{\mu}}\right)\right]^{\kappa/(\kappa-1)}. \tag{25}$$

The complete equations capture the physical phenomena of jamming (i.e., the absence of flow), which occurs for stresses smaller than a yield stress σ_y that satisfies Eq. (11). Otherwise, the behavior is very similar to our previous results for the nonlinear free-volume equations. For nonvanishing shear rates, we can again define $\sigma^*>\sigma_y$ as the solution of

$$\frac{\alpha E_0}{E_1}\left(\sigma^*\sinh\left(\frac{\sigma^*}{\bar{\mu}}\right)-\mu_0\cosh\left(\frac{\sigma^*}{\bar{\mu}}\right)\right)=1 \tag{26}$$

and $\dot{\epsilon}^*=\dot{\epsilon}(\sigma^*)$. Again, for $\kappa<1$, the stress vs strain rate relation is decreasing, and for $\kappa>1$, it is increasing. Again, the range of strain rates where steady sliding is reached is bounded by $\dot{\epsilon}<\dot{\epsilon}^*$. We see from Eq. (25) that the STZ dynamics do not significantly change the sliding properties as soon as the relevant values of the stress are large compared to σ_y. This situation is particularly relevant for stick-slip instabilities, which occur for $\kappa<1$, in the low velocity, large stress regime.

B. Transient dynamics characterizing the approach to steady sliding

Next we describe transient effects associated with discrete jumps in the applied strain rate. Both the initialization of the system, as well as several common experimental procedures probing transients under controlled conditions, can be described in this general framework. We first consider the initial, waiting-time-dependent transients associated with starting the system from rest. This is followed by an examination of the experimental protocol, referred to as stop-start or slide-hold-slide tests, in which the system is prepared in the steady state before the waiting time begins. For this analysis, we will focus on the linear and nonlinear free-volume equations. Inclusion of the STZ terms does not quantitatively alter the results.

1. Transient dynamics upon start-up

In the absence of forcing, $\sigma=0$, the linear and nonlinear free-volume equations are equivalent. From Eq. (10) [or Eq. (13), or Eq. (15)], the free volume χ relaxes to 0. The late stages of this relaxation (as the waiting time t_w, goes to ∞) are logarithmic in time:

$$\chi(t_w)\simeq\frac{\kappa}{\log_{10}(E_1t_w)}. \tag{27}$$

Simultaneously, as the system becomes increasingly compact, the effective "viscosity" [Eq. (16)] increases:

$$\eta(t_w)\equiv\frac{1}{E_0}\exp\left[\frac{1}{\chi}\right]\simeq\frac{1}{E_0}(E_1t_w)^{1/\kappa}. \tag{28}$$

The immediate consequence of this time-dependent relaxation is that the material displays an age-dependent initial value of the stress when shear is subsequently applied.

This is illustrated in Fig. 1 where we plot χ and σ as a function of time, obtained from the integration of Eq. (1) coupled to Eqs. (12) and (13). Distinct peaks correspond to samples of different ages at the onset of the applied strain rate. In every case, the system is initialized at $t=0$ with a large value $[\chi(t=0)=10]$ of the free volume. From time $t=0$ to $t=t_w$, the free volume relaxes in the absence of applied shear. At time $t=t_w$, a strain rate $\dot{\epsilon}$ is suddenly applied and held constant from that time on. For each curve, the value of t_w corresponds to the time when stress begins to ramp up.

The initial increase of the stress is due to the fact that χ has relaxed to a relatively small value during the waiting

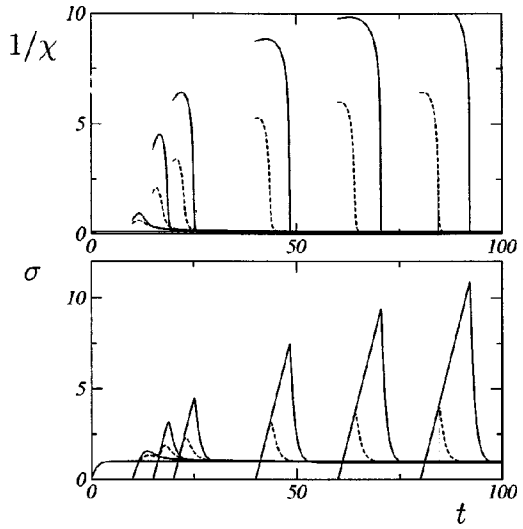

FIG. 1. Transient dynamics upon start-up from the integration of Eq. (1) coupled to Eqs. (12) and (13), with $E_0=E_1=\alpha=1$. σ and $\bar{\mu}$ are in units of 10^6 N/m^2; time is made dimensionless by the choice of E_0, E_1, and α. From Eq. (18), $\dot{\epsilon}^*=1$, and the applied strain rate is $\dot{\epsilon}=0.9$. Results for $\kappa=0.8$ (solid lines) and $\kappa=1.2$ (dashed lines) are shown. No stress is applied during the initial density relaxation of the material from $t=0$ to $t=t_w$, marked by the increase of stress. At t_w the strain rate is suddenly applied and the ensuing dynamics of $1/\chi$ (top) and σ (bottom) are displayed. Here smaller values of κ (i.e., $\kappa=0.8$) lead to a larger value of the dynamical yield strength, which results from the fact that a smaller value of χ (more compact state) is reached during the waiting period.

time, resulting in a high effective viscosity, which resists rapid deformation of the material. When the stress gets large, the free volume increases. The system dilates, and the shear deformation rate increases suddenly, resulting in the observed stress drop.

2. Stiff apparatus

To provide analytical estimates of the age dependence of the peak stress, we take the limit of an infinitely stiff apparatus, $\mu\to\infty$. When a fixed shear rate is imposed after some waiting time t_w, the interfacial material resists with a force which is an increasing function of age t_w. For the linearized equation (14), the stress upon start-up reads

$$\sigma_{\mathrm{start}}(t_w)=\frac{1}{E_0}(E_1 t_w)^{1/\kappa}\dot{\epsilon}. \tag{29}$$

The response is viscous, with an instantaneous initial viscosity which increases as a power of the waiting time. For the nonlinear free-volume equations (12), the power-law dependence is replaced by a logarithm. For large t_w, the force upon start-up is

$$\sigma_{\mathrm{start}}(t_w)\simeq\frac{\bar{\mu}}{\kappa}\log_{10}(E_1 t_w)+\bar{\mu}\log_{10}\left(\frac{\dot{\epsilon}}{E_0}\right). \tag{30}$$

This logarithmic dependence is a direct consequence of the assumption that transformation rates $R_\pm$ depend exponentially on stress [i.e., are proportional to $\exp(\pm\sigma/\bar{\mu})$]. A remarkable consequence arises from this assumption: the slopes of σ_{start} vs $\log_{10}(t_w)$ and σ vs $\log_{10}\dot{\epsilon}$ in steady state have a ratio given by $\kappa-1$. Expression (30) is consistent with experimental observations, although existing SFA data [29,33] do not present a clear scaling for the long waiting time behavior of the peak stress. A logarithmic scaling of the peak stress, however, can be observed in the dry friction measurement of joint plasticity by Bureau *et al.* [36]: the slope of σ_{start} vs $\log_{10}(t_w)$ is of order 10^{-3}. The ratio of the slopes of σ_{start} vs $\log_{10}(t_w)$ and σ vs $\log_{10}\dot{\epsilon}$ in steady state extracted from their data is consistent with κ of order 1, which is reassuring as this quantity is a ratio of two activation volumes.

A common observation in both classes of experiments is that the increase of the peak stress over time depends sensitively on the level of shear stress that is sustained during aging. With the SFA, the peak stress has been observed to decrease with increasing stress level [29]. In our framework, this is consistent with the idea that shear induces some amount of dilatancy, i.e., of rejuvenation. Sustaining a stress during the waiting time arises in our model through the term $\alpha E_0\exp(-1/\chi)\sigma^2$ in Eq. (10) [or Eq. (13), or Eq. (15)]. For fixed time and increasing levels of stress, the variable χ reaches larger values than in the absence of stress. Hence the stress peak is smaller.

In the experiments by Bureau *et al.* the slope of σ_{start} vs $\log_{10}(t_w)$ increases as the level of shear stress sustained during the waiting time is increased. This shear-stress-induced acceleration of aging dynamics in dry friction experiments can be understood in two different ways.

(i) Subdominant stress dependencies of the activation volumes, $\kappa=v_1/v_0$, may slightly decrease with shear stress. This would correspond to the idea that shear stress activates the relaxational dynamics of aging.

(ii) Since we have no control on the orientation of individual asperities in this geometry, part of the shear stress sustained during the waiting time may be transformed into normal stress by very small amounts of elastic deformation or creep, tilting the orientation of joints between individual asperities. Such a transfer would affect the value of $\bar{\mu}$—which is expected to depend on the normal load—at least just upon start-up, and hence the value of the peak stress. The existence of transfers between shear and normal stress cannot be identified in dry friction measurements. The SFA could be helpful in separating the different contributions by studying how aging depends on the normal load.

3. Stop-start tests

The characteristics of glassy materials depend sensitively on sample age and preparation methods. It is therefore important to focus on experimental protocols in which the initial state can be relatively well defined. One common experimental convention which aims to control the initial state involves starting from steady sliding motion. The initial state of the material is determined by the driving velocity. In velocity step experiments the drive velocity undergoes discrete changes from one value to another, and the transient response is monitored. This was one of the original protocols used to investigate the correspondence between rate and state

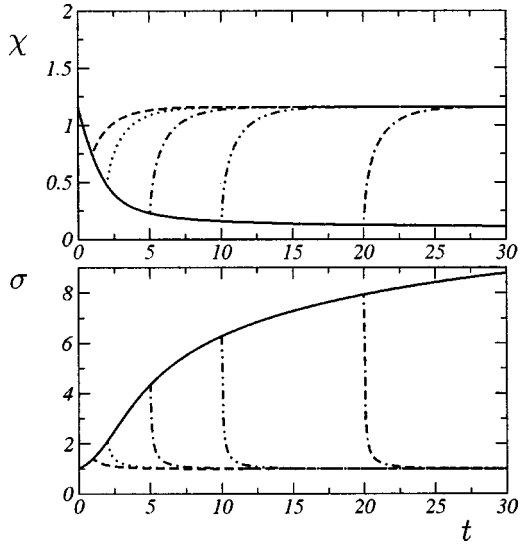

FIG. 2. Numerical integration of Eqs. (12) and (13) during stop-start tests for shear rate $\dot{\gamma}=\dot{\epsilon}=0.5$. Parameters are $E_0=E_1=\alpha=\mu=1$, and $\kappa=0.8$; σ and $\bar{\mu}$ are in units of 10^6 N/m^2; time is made dimensionless by the choice of E_0, E_1, and α. For each curve, the applied shear halts for a time t_w, after which it is suddenly reapplied. The dynamics of χ (top) and σ (bottom) are displayed. The solid lines indicate the relaxation of χ in the absence of shear, and the value of σ upon start-up. Different line styles are used for different t_w.

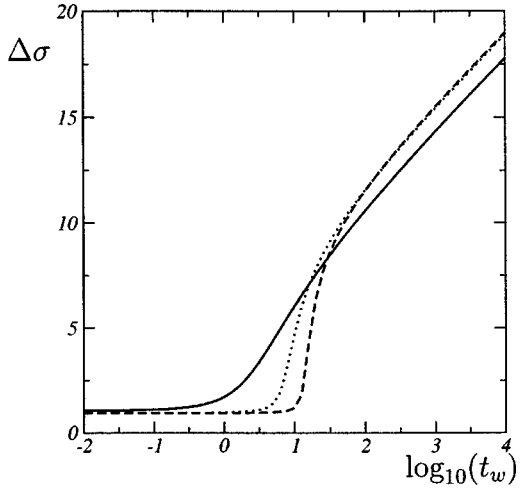

FIG. 3. Peak stress $\Delta\sigma$ as a function of waiting time t_w, from integration of Eqs. (12) and (13). Parameters are $E_0=E_1=\alpha=\mu=1$, and $\kappa=0.8$, whence $\dot{\epsilon}^*=1$; σ and $\bar{\mu}$ are in units of 10^6 N/m^2; time is made dimensionless by the choice of E_0, E_1, and α. Different shear rates have been used: $\dot{\gamma}=\dot{\epsilon}=0.3$ (solid line), 0.9 (dotted line), and 0.99 (dashed line). Approaching $\dot{\epsilon}^*=1$, a latency time interval becomes increasingly well defined, indicating the increasing importance of free-volume dynamics beyond the small χ domain, where log-time relaxation of the free volume holds.

laws and dry friction experiments [41,42] and was recently investigated for lubricated contacts [29]. Another protocol, referred to as stop-start or slide-hold-slide experiments, involves preparing the system in a constant velocity steady state, then suddenly stopping the drive and letting the system relax for a time t_w, and finally restarting at the initial velocity. This latter protocol has been studied extensively in boundary lubrication [5,15,31] and for the plastic response of single asperities at the contact between rough surfaces [36].

This stop-start protocol grants direct access to the aging process from a well controlled initial state. Stop-start tests are depicted in Fig. 2, based on numerical integration of Eqs. (12) and (13) in the limit of an infinitely stiff apparatus. Here χ and σ are plotted as functions of time. The initial value of χ corresponds to the steady state at a given shear rate $\dot{\epsilon}=0.5$. When the external drive halts (the "stop" phase), χ relaxes to a smaller value, as the lubricant becomes more compact. The same shear rate in then suddenly reapplied (the "start" phase) after different waiting times. In this $\mu\to\infty$ limit, $\dot{\gamma}=\dot{\epsilon}$, and the stress immediately takes its peak value, where the position of the peak marks the waiting time for each curve. After start-up, the free volume increases, due to the transfer of the work of shear forces into enthalpy. This results in a decrease of the viscosity η, accompanied by a decay of the stress with time.

The solid line in Fig. 2 marks the envelope of all response peaks, and thus defines the peak stress as a function of the resting time t_w. Experimentally, for short waiting times, Yoshizawa and Israelachvili [15] observed that for certain lubricants the corresponding curve exhibits a well defined latency time. That is, there is a threshold in the waiting time, below which no increase in the stress is observed. For longer waiting times, Drummond and Israelachvili [29] and Gourdon and Israelachvili [33] found that the difference $\Delta\sigma$ between the peak value of the stress and the steady state value (the so-called "stiction spike") increases as $\Delta\sigma\sim\log_{10}(t_w)$ for large t_w.

Both the short and long time behavior is reproduced by the nonlinear free-volume equations, as shown in Fig. 3 for different values of the driving velocity. Note that the latency time (roughly associated with the rapid rise of $\Delta\sigma$) becomes increasingly sharply defined at high drive velocities. This follows from the fact that at high velocities, approaching the limiting shear rate $\dot{\epsilon}^*$, the stationary value of the free volume is large, and hence free-volume activation factors [which scale as $\exp(1/\chi)$] are essentially constant. Therefore, the free volume χ nearly decouples from the relation between stress and strain rate: if the external drive is stopped during a short time interval, χ relaxes, but the changes in χ have little effect on the dynamic viscosity η. When the shear is applied again, the relation between stress and strain rate is still very close to steady state, and only a very faint peak is observed.

This effect has dramatic consequences at high shear rates. For $\dot{\epsilon}>\dot{\epsilon}^*$, χ is driven toward high values corresponding to a fluidized state. In our model, χ steadily increases at a rate E_1. After stopping the drive, the time required for χ to reenter the aging regime is proportional to the time it was driven out of equilibrium. This phenomenon should thus result in a latency time which depends linearly on the shearing time prior to stopping.

This strain dependence of the latency time is a direct consequence of the fact that in our model χ does not saturate in the limit of high shear rate. However, saturation should arise from weak density dependence of the constants. Schemati-

cally, we can see how our picture might be altered by incorporating this effect, by adding a constraint that χ cannot increase beyond a large value $\chi_\infty \gg 1$. At high shear rate χ would ultimately saturate at χ_∞. When the driving is stopped the time required for χ to relax to values of order κ (the latency time) is of order χ_∞/E_1.

We see here two related yet different types of latency. In both cases a latency interval emerges due to the weak dependence of the activation factors for large values of χ. For $\dot{\epsilon} < \dot{\epsilon}^*$, χ reaches a true steady state. For $\dot{\epsilon} > \dot{\epsilon}^*$, χ either does not converge or reaches a very high saturation value χ_∞. In all cases, because of the decoupling of χ from the stress-strain relation, measurements of stress become unreliable to assert that the system has reached a steady state. χ may be nonstationary. In this case, the latency interval emerging from this underlying dynamics should depend on the detailed preparation of the system, in particular on the amount of shear before stopping.

In experiments, typical values of the latency time are of order 1 s [15,29,31]. Because the underlying microscopic time scale parameters in our model are not fixed a priori, such values can be interpreted in several different ways in the context of our model. (i) By an appropriate scaling of the parameters, in particular, E_1: scaling E_1 translates the curves horizontally in Fig. 2. (ii) Because seconds are also the time necessary to prepare the system in a state believed to be steady, the latency time may reflect the preparation period, while the dynamics of χ remain nonstationary. (iii) Assuming a saturation value χ_∞ for χ would prescribe a latency time χ_∞/E_1, which could be of order seconds. We cannot distinguish between these possibilities at the present time. However, we remark that measurements of latency times are often accompanied by very large fluctuations [15,29,31]. Our study suggests that the nonstationary dynamics of an underlying state variable can be responsible for these fluctuations. If this is the case, experimental data could be regularized by controlling the amount of shear the system undergoes at a high velocity, starting from a well controlled initial state—prepared, for example, by first shearing at a lower velocity.

C. Instability and transition to stick-slip

Here, we show that our constitutive equations not only account for the existence of stick-slip behavior at low drive velocity, but reproduce the shape of the stick-slip cycle with remarkable accuracy. They also account for the existence of continuous and discontinuous transitions to stick-slip depending on the stiffness of the apparatus, and, in some cases, chaos in the neighborhood of the transition. For this analysis, the nonlinear free-volume equations will be sufficient to characterize the transition from stick-slip to steady sliding and the nature of the bifurcation. The full set of coupled constitutive equations, including the STZ, preserve the phase boundaries described by the free-volume equations. However, STZ effects (particularly those introducing another dimension to the dynamical system) are required to capture chaotic phenomena.

1. Stick-slip motion: Shape of the pulse

At low drive velocities, and for a sufficiently compliant apparatus, rather than sliding at constant velocity, the interface exhibits stick-slip motion. We begin our analysis of this motion by illustrating a typical stick-slip cycle obtained from numerical integration of Eq. (1) coupled with the constitutive equations (12) and (13). In Fig. 4 we plot the time series of χ and σ during stick-slip. As in the experiments, stick-slip cycles appear qualitatively similar to stiction peaks. However, stick-slip arises when the driving motion is constant, unlike stiction peaks in stop-start tests, which represent transient responses to time varying slide-hold-slide drivers and are typically monitored in a regime where the steady state motion corresponds to constant velocity sliding. Stick-slip arises due to an internal instability of the material at a given shear rate. Rather than sliding at that steady rate, the material alternates between "sticking" and "slipping." During the stick phase the free volume decreases to a value that is small enough to hinder the relative displacement of lubricated surfaces, during which time the material creeps at a rate that is too slow to keep up with the external drive. Consequently, the stress builds up. When it becomes large enough to trigger dilatancy, the slip phase begins, χ increases suddenly, and the stress is released during rapid sliding motion.

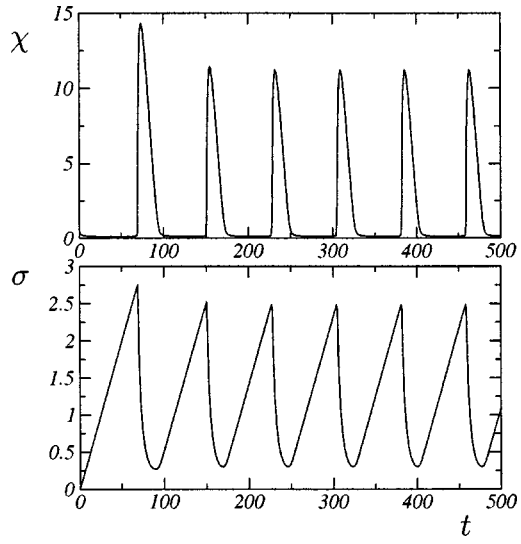

FIG. 4. Stick-slip dynamics obtained from numerical integration of Eqs. (1), (12), and (13) for a fixed strain rate $\dot{\epsilon}=0.2$ and stiffness $\mu=0.2$. Parameters are $E_0=E_1=\overline{\mu}=\alpha=1$, and $\kappa=0.8$; σ and $\overline{\mu}$ are in units of 10^6 N/m^2 time is made dimensionless by the choice of E_0, E_1, and α. The initial value of the free volume is $\chi=1$. The regime of steady plastic deformation is unstable and leads to stick-slip motion. Fast relaxations of the stress result from sudden dilatancy of the material.

In Fig. 5 the same data are represented in a plot of σ versus $\dot{\gamma}$, which compares quite favorably with typical cycles observed by Drummond and Israelachvili [29].

2. Characterization of the Hopf bifurcation

With decreasing velocity and for a compliant apparatus, our constitutive equations exhibit a Hopf bifurcation separating steady sliding from stick-slip dynamics. The locus of bifurcation points defines a phase boundary in the μ (stiffness) vs $\dot{\epsilon}$ (strain rate) plane. A systematic analysis of the emergence of stick-slip motion is easily performed for the

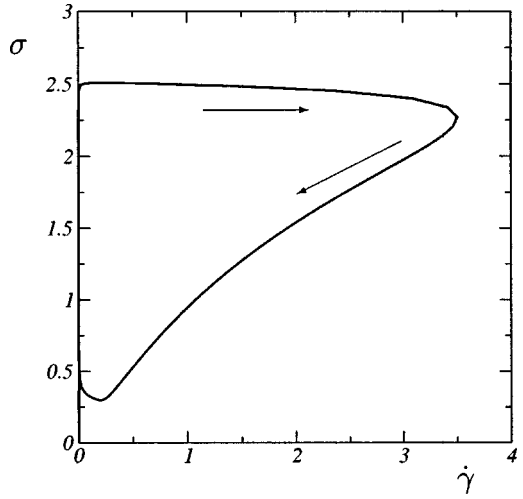

FIG. 5. Stick-slip cycle from the data of Fig. 4. Arrows indicate the direction in which the stick-slip cycle is followed. The ramps on Fig. 4 correspond here to the increase of σ at vanishing $\dot{\gamma}$. The plastic strain rate suddenly increases at almost constant σ before the friction force starts to decrease.

stress-linear version of the constitutive equations. The details are given in the Appendix. The critical stiffness defining the Hopf bifurcation point for Eqs. (1), (12), and (13) is given by

$$\mu_{\mathrm{Hopf}} = \frac{E_1}{E_0}\frac{1-\kappa}{(\kappa+1)^2}\left(\frac{\alpha\dot{\epsilon}^2}{E_0E_1}\right)^{(\kappa-1)/(\kappa+1)} \ln\left[\frac{\alpha\dot{\epsilon}^2}{E_0E_1}\right]^2. \quad (31)$$

Solving for μ as a function of $\dot{\epsilon}$, with all other parameters held fixed, defines the phase boundary in the $(\mu,\dot{\epsilon})$ plane, below which steady sliding becomes unstable (see Fig. 6).

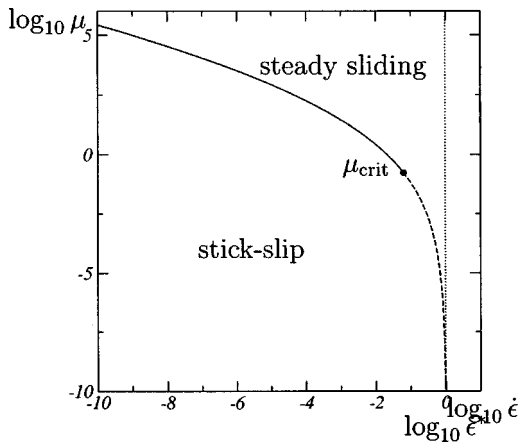

FIG. 6. Phase diagram for Eqs. (1) and (14), and (15), and $\kappa<1$, in the $\log_{10}\dot{\epsilon}-\log_{10}\mu$ plane. The dotted line indicates the limit velocity $\dot{\epsilon}^*$ beyond which χ diverges. The solid and dashed lines denote the curve μ_{Hopf} below which steady sliding motion is unstable; μ_{Hopf} vanishes at $\dot{\epsilon}=\dot{\epsilon}^*$. The solid part of this line corresponds to points where the transition to stick-slip is continuous (supercritical) while the dashed line corresponds to points where the transition is discontinuous (subcritical). When the transition is discontinuous, there is a zone of bistability, which lies above the dashed line.

Our curve exhibits the same convexity as available experimental data [31,47]. Additional experiments are needed to provide a quantitative experimental characterization of the curve.

Experimental data also suggest that different types of transitions between stick-slip and steady sliding are possible. The transition may be continuous (approaching the phase boundary the amplitude of stick-slip motion decreases continuously to zero as drive velocity is increased) or discontinuous (there is an abrupt change from finite amplitude stick-slip spikes to steady sliding as drive velocity is increased). Continuous transitions correspond to supercritical Hopf bifurcations, and discontinuous transitions correspond to subcritical bifurcations. The latter case is typically accompanied by hysteresis (i.e., coexistence of stick-slip and steady sliding, such that a steady decrease in the drive velocity results in a transition to stick-slip at a lower strain rate than that associated with the transition to steady sliding associated with increasing velocity from the stick-slip phase). This feature is observed in both lubricated friction [31] as well as dry interfaces. In the latter case it is better characterized [47], although the physical origin of the similarity (if indeed it persists upon more detailed experimental investigations) remains unclear. For both cases to date analytical models have failed to capture the existence of both super- and subcritical Hopf bifurcations.

The transition point separating super- and subcritical Hopf bifurcations on the phase boundary in the $(\mu,\dot{\epsilon})$ plane depends on third order terms in a normal expansion of the dynamical system around the steady state. Therefore, this property offers a particularly stringent test of the constitutive equations. We have performed the analysis of the system (1), (12), and (13). Our analysis defines a point

$$\mu_{\mathrm{crit}} = \frac{E_1}{E_0}\frac{e^{-\kappa+\sqrt{2-2\kappa+\kappa^2}}}{1-\kappa}(\kappa-\sqrt{2-2\kappa+\kappa^2})^2 \quad (32)$$

on the Hopf line, which is drawn in Fig. 6. Above, and on the left of this point, the Hopf bifurcation is supercritical (continuous); below, and on the right of it, the bifurcation is subcritical (discontinuous).

The shape of the phase boundary as well as the types of transitions and even their relative placement in the phase diagram are consistent with current experimental observations. However, a complete and quantitative characterization of the phase diagram for boundary lubrication remains an open challenge experimentally. Overcoming obstacles associated with the limited range of stiffness that can be probed with existing techniques will enable key observations which can be compared with both the contrasting case of dry friction experiments and the theoretical results presented here.

D. Chaotic stick-slip

Drummond and Israelachvili [29] observed that in some cases stick-slip motion became erratic in the neighborhood of the transition. These authors identified the erratic motion as *chaotic*, based on the analysis of experimental time series. Their results were indeed suggestive of positive Lyapunov exponents. However, methods to identify chaos based on

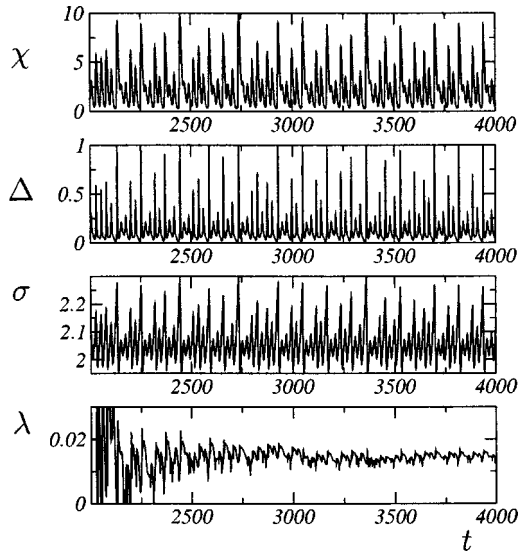

FIG. 7. Chaotic motion: Δ, χ, σ, and λ are plotted as functions of time t for Eqs. (1), (7), (8), and (10) for parameters $E_0=0.5$, $E_1=1$, $\epsilon_0=1$, $\alpha=2$, $\mu_0=0.5$, $\bar{\mu}=0.5$, $\mu=0.14$, $\kappa=0.8$, and $\dot{\epsilon}=0.14$; σ and $\bar{\mu}$ are measured in units of 10^6 N/m^2. The asymptotic limit reached by $\lambda(t)$ is the largest Lyapunov exponent, which is clearly positive, indicating chaos.

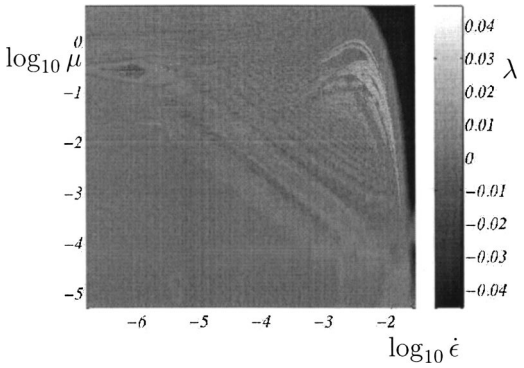

FIG. 8. Two-dimensional plot of the asymptotic Lyapunov exponent in the $[\log_{10}(\dot{\epsilon}),\log_{10}(\mu)]$ plane obtained from numerical integration of Eqs. (1) and (7)–(10). The grayscale on the right gives the maximum value of the Lyapunov exponent λ, as defined in Eq. (33). Negative values of the Lyapunov exponent appear in dark shades: they correspond to steady sliding. The vertical asymptote of the phase boundary as $\log_{10}(\mu)\to-\infty$ (i.e., roughly the right edge of the figure) corresponds to ϵ^*. Periodic stick-slip is shown in medium gray, corresponding to vanishing of the Lyapunov exponent. Chaotic behavior is associated with positive values of the Lyapunov exponent, which appear here in light shades. Chaotic regions of stick-slip are separated by windows of periodic motion.

analysis of an individual experimental time series are necessarily approximate and inconclusive, and alone are insufficient to guarantee that the erratic motion is chaos as opposed to some form of noise amplification.

Given these uncertainties, models can play a special role in helping to differentiate between mechanisms which may lead to chaos vs other modes of irregular motion. Here we study the full set of nonlinear constitutive equations (1) and (7)–(10), which include the STZ state variables. The dimension of this dynamical system is 3, which is the minimum requirement for chaos. As shown below, over a restricted range of parameters, the model admits chaotic solutions, characterized by irregular stick-slip and positive Lyapunov exponents. Because these equations are deterministic, noise amplification is ruled out as a source of irregular motion in the model.

In order to measure Lyapunov exponents we directly integrate the equations of motion of a Lyapunov vector $u(t)$ in the tangent space (see, e.g., [88]). The largest Lyapunov exponent λ is estimated from the long time behavior of the norm of this vector:

$$\lambda = \lim_{t\to\infty} \frac{1}{t} \log_{10} \|u(t)\|. \tag{33}$$

For this numerical study, we used a fourth order Runge-Kutta algorithm with fixed and variable time steps. We checked that the results do not change qualitatively as a function of the precision of our numerical method, as long as the precision is sufficiently high.

Figure 7 shows typical traces in the chaotic regime. The three variables σ,Δ,χ as well as the value of

$$\lambda(t) \equiv \frac{1}{t} \log_{10} \|u(t)\| \tag{34}$$

are shown. These data illustrate that chaotic stick-slip can arise in this system. Chaos results from the interplay between the dynamics of the variable Δ, which characterizes the anisotropy of the molecular packing, and the variable χ, which characterizes the dilatancy of this packing.

Further investigation reveals that the range of parameters where chaos (i.e., at least one positive Lyapunov exponent) is observed is restricted to a relatively compact area of the μ vs $\dot{\epsilon}$ phase diagram, which is close to but not overlapping the transition from stick-slip to steady sliding, in a region near the critical point separating sub- and supercritical Hopf bifurcations. This relatively restricted range is not surprising. Since chaos requires the dynamical system to be three dimensional, it may disappear as soon as one variable is enslaved to another. In our case, this decoupling may occur either when the time scales of the dynamics of Δ and χ are well separated from each other or when the absolute value of Δ becomes negligible in Eq. (7).

To illustrate the chaotic domain, in Fig. 8 we present a two-dimensional image illustrating the value of the maximum Lyapunov exponent as a function of the parameters μ and $\dot{\epsilon}$. In the grayscale map, negative values of the Lyapunov exponent appear in dark shades and indicate that the dynamics has reached a stable fixed point. This corresponds to steady sliding motion at constant χ. Such solutions exist between the Hopf bifurcation and the $\dot{\epsilon}=\dot{\epsilon}^*$ line (recall that, for $\dot{\epsilon}>\dot{\epsilon}^*$, χ diverges, and our theory breaks down). In the grayscale map, medium gray corresponds to a zero value of the Lyapunov exponent. The value $\lambda=0$ indicates that the dynamics reach a time translation invariant manifold. This is

indicative of stick-slip regimes, which exhibit a periodic limit cycle. Lighter shades correspond to positive values of the Lyapunov exponent: for these values of the parameters, the dynamics is chaotic.

Chaotic motion is associated with positive Lyapunov exponents which appear as light gray in Fig. 8. They occur within the stick-slip portion of the phase diagram, near the transition between super- and subcritical bifurcations. As shown in the figure, in the model this behavior is clearly separated from the Hopf boundary by a narrow range of regular stick-slip. The close proximity of the chaotic zone to the Hopf bifurcation may explain the fact that experimentally it appears that, when chaotic stick-slip is observed, it merges continuously into the Hopf transition. While our equations predict a regular Hopf bifurcation to periodic stick-slip, with chaotic stick-slip resulting from secondary instabilities, the intermediate periodic regime occurs over a sufficiently narrow range that it may be difficult to differentiate experimentally between this case and a case in which the Hopf transition takes place directly via chaotic stick-slip.

V. CONCLUSION

We have shown that a limited set of constitutive equations capture at least qualitatively a wide variety of phenomena observed experimentally in single asperity, boundary lubricated friction. Most of the phenomena are captured by the dynamics of a single state variable identified here as the free volume. In steady sliding, the free-volume dynamics account for the existence of velocity-weakening or velocity-strengthening friction laws, involving mixed power laws and logarithmic dependences. In stop-start experiments, logarithmic increases in the peak stress with increasing hold time result from the relaxation of the free volume, whereas for short hold times a latency time emerges from the nonlinearity of the transition rates. The dynamics of the free volume also accounts for the existence of a transition from steady sliding to stick-slip as the drive velocity is decreased and for the presence of both continuous and discontinuous transitions, depending on the stiffness of the driving apparatus. Finally, the complete set of equations where the free volume couples to the dynamics of STZs accounts for the emergence of chaotic behavior close to the stick-slip transition.

Our present work is in sufficiently close qualitative agreement with experiments to warrant a further round of more quantitative experimental vs theoretical comparisons. Our work leads to clear predictions for the friction in steady sliding regimes, and the transition to stick-slip as a function of the compliance. Available experimental data provide steady sliding friction over a limited range of velocities and a collection of stick-slip cycles at low velocities for a given interfacial material, most often for a unique value of the compliance. Available measurements of power-law or logarithmic relationships between force and driving velocity are not sufficient to validate or invalidate a set of constitutive equations. In principle, we could attempt to directly fit cyclic stick-slip data, but in practice this is extremely difficult, requiring additional assumptions about initial values of one or more internal variables. What information can we thus use to compare theory and experiments? Compliance is included in the model at a low cost in terms of the assumptions required, yet provides a large panel of predictions that magnify the sensitivities of the constitutive equations and the microscopic assumptions of the theory. The location of the transition to stick-slip, its dependence on compliance, and the type of transitions to stick-slip are important predictions of our model that present opportunities for more detailed comparisons with experimental data. Drummond and Israelachvili [29] have been able to study transitions to stick-slip for a few values of the compliance over a limited range. We hope this initial, exploratory study will be followed by a more complete set of measurements to compare with our predictions.

Recent experimental results by Gourdon and Israelachvili [33] have focused on the temperature and pressure dependence of the transition to stick-slip. While these variables are more accessible experimentally than compliance, they present greater challenges for theory, and cannot be addressed directly here because temperature and pressure do not appear explicitly in the constitutive laws we consider. However, a recent derivation of similar equations [57] provides theoretical insights into the temperature and pressure dependence, suggesting future opportunities to extend our current analysis in this direction.

A quantity that arose in several contexts throughout this paper was the critical strain rate $\dot{\varepsilon}^*$, beyond which the value of χ cannot reach steady state. In our equations, above $\dot{\varepsilon}^*$, χ diverges with time, because the internal (bounded transition rate) relaxation dynamics cannot keep pace with the rate at which energy is added to the system. While an actual divergence of χ may be impeded by various physical mechanisms (which we did not attempt to incorporate), we believe that the existence of a change of behavior at some high strain rate is physically meaningful and likely to be an important property that is closely related to the existence of a latency time in stop-start tests. Because transformation rates are bounded, at high strain rates the underlying state variable is expected to decouple from the relation between stress and strain rates. This decoupling has several consequences. (i) Since the shear rate is only weakly dependent on state variables, and since it is an increasing function of the stress, velocity strengthening behavior emerges. (ii) The state variable is hidden, its value cannot be deduced from the relation between stress and strain rate, and measurements of apparent steady relationships between stress and strain rate may not correspond to a true steady state. (iii) The hidden value of the state variable depends on the strain. (iv) When the deformation is interrupted, the state variable requires some time before it reaches a sufficiently low value for it to make a measurable impact that can be probed by the emergence of a transient peak (i.e., a stiction spike) in stress. In this case, the latency time becomes a function of the overall strain. If a high strain rate fixed point is reached by the state variable, this dependence disappears, and the latency time should depend only on the strain rate. It would therefore be particularly interesting to see whether the underlying dynamics of a state variable can be probed in experiments close to and above $\dot{\varepsilon}^*$ and whether it is consistent with either the emergence of a high strain rate fixed point, or with unstationary dynamics of the state of the lubricated contact. Velocity

strengthening has not been observed with the SFA, probably because of intrinsic limits due to the finite scan length. Therefore, it is likely that the high strain rate regimes we discuss here cannot be directly accessed with this experimental setup. However, velocity strengthening has been observed in numerics [7] and recently in the experiments [36] by Bureau and co-workers. This latter experimental setup is constructed to allow sliding over longer distances, and provides access to higher drive velocities than those available with the SFA. It thus may present opportunities to probe some phenomena that arise at high velocities.

Finally, we note that the constitutive equations presented here are derived from heuristic assumptions, which extend STZ theory to the rearrangements occurring inside the sheared material in a lubricated contact. Although our approach is phenomenological, it relies on a specific picture of the microscopic and mesoscopic mechanisms of deformation, and thus forms a bridge between macroscopic, empirical descriptions and a fundamental understanding of the microscopic physics. The STZ picture of plastic rearrangements occurring in localized zones is supported by numerical observations [58]. However, it would be useful to also image rearrangements in experimental situations. Although the SFA provides a very well controlled environment at the microscopic level, it seems unlikely that such atomistic imaging of the lubricant could be performed. Other materials are more likely candidates for such observations. Indeed, the picture of elementary rearrangements that emerges here is not limited to lubricants, but is expected to apply to a wide range of amorphous materials, in particular colloidal suspensions and granular materials. Indeed, recent experiments by Gollub and co-workers have imaged local rearrangements in granular bead packs forming the interfacial material in friction measurements. These experiments also exhibit stick-slip at low drive velocities, and a transition to steady sliding as the driving rate is increased [51–53]. A further theoretical challenge associated with these measurements arises because slip does not occur homogeneously in the material, but rather is primarily restricted to a relatively narrow dilating region near the top of the bead pack. We expect the results presented here may extend to other types of amorphous materials, but in situations when strain localization does not preempt the application of a homogeneous description. Colloids and granular materials may provide simultaneous access to macroscopic rheological properties and microscopic imaging of elementary rearrangements.

ACKNOWLEDGMENTS

This work was supported by the W. M. Keck Foundation, and the NSF Grant No. DMR-9813752, and by EPRI/DOD through the Program on Interactive Complex Networks.

APPENDIX: HOPF ANALYSIS

We present here the details of the calculation of the Hopf bifurcation for the stress-linear free-volume constitutive equations (14) and (15). The complete dynamics studied can be rewritten as

$$\dot{\sigma} = \mu\left(\dot{\epsilon} - E_0 \exp\left[-\frac{1}{\chi}\right]\sigma\right), \tag{A1}$$

$$\dot{\chi} = -E_1 \exp\left[-\frac{\kappa}{\chi}\right] + \alpha E_0 \exp\left[-\frac{1}{\chi}\right]\sigma^2. \tag{A2}$$

The calculation of the Hopf bifurcation point is straightforward: it amounts to considering the trace of the Jacobian of this dynamical system. However, the calculation identifying the critical Hopf point μ_{crit} dividing the sub- and supercritical bifurcation lines requires more lengthy calculations and benefits from the introduction of simplifying notation. Let us write the equations as

$$\dot{\sigma} = \mu[\dot{\epsilon} - f_1(\chi)\sigma], \tag{A3}$$

$$\dot{\chi} = -f_2(\chi) + \alpha f_1(\chi)\sigma^2, \tag{A4}$$

and perform the analysis in this more general framework.

The stationary solution is determined by

$$\sigma^2 \equiv S(\chi) = \frac{f_2(\chi)}{\alpha f_1(\chi)} \tag{A5}$$

and

$$\dot{\epsilon}^2 \equiv E(\chi) = \frac{f_1(\chi) f_2(\chi)}{\alpha}, \tag{A6}$$

where the functions E and S have been introduced for future convenience. In the case of Eqs. (A1) and (A2), these functions are

$$E(\chi) = \frac{E_0 E_1}{\alpha} \exp\left[-\frac{\kappa+1}{\chi}\right] \tag{A7}$$

and

$$S(\chi) = \frac{E_1}{\alpha E_0} \exp\left[-\frac{\kappa-1}{\chi}\right]. \tag{A8}$$

The Jacobian of this dynamical system reads

$$J = \begin{pmatrix} -\mu\, f_1(\chi) & -\mu\, f_1'(\chi)\sigma \\ 2\,\sigma\, f_1(\chi) & -f_2'(\chi) + \sigma^2 f_1'(\chi) \end{pmatrix}, \tag{A9}$$

and around the stationary solution the eigenvalues of the Jacobian satisfy

$$\lambda^2 + \lambda\sqrt{\frac{E(\chi)}{S(\chi)}}[\mu + \alpha\, S'(\chi)] + \alpha\,\mu\, E'(\chi) = 0. \tag{A10}$$

The Hopf bifurcation occurs when

$$\mu = -\alpha S'(\chi) \tag{A11}$$

at any point where $E(\chi)$ is strictly increasing. In our case, E is always an increasing function of χ, and S is a decreasing function of χ if and only if $\kappa<1$. If S is an increasing function of $\chi(\kappa>1)$—which also means that $S\circ E^{-1}$ is an increasing function of $\dot{\epsilon}$, there is no Hopf bifurcation, and the steady sliding motion is stable. If $\kappa<1$, S is a decreasing function

of χ; for any $\dot{\epsilon}$, there is a critical value of μ where the system undergoes a Hopf bifurcation:

$$\mu_{\mathrm{Hopf}} = -\alpha S'[E^{-1}(\dot{\epsilon}^2)] = \frac{E_1}{E_0}\frac{1-\kappa}{(\kappa+1)^2}\left(\frac{\alpha\dot{\epsilon}^2}{E_0E_1}\right)^{(\kappa-1)/(\kappa+1)}\ln\left[\frac{\alpha\dot{\epsilon}^2}{E_0E_1}\right]^2.$$

In order to determine the type of Hopf bifurcation (super- or subcritical), we write our nonlinear system of ordinary differential equations (ODE's) in normal form. For this purpose, we look for the linear operator T which transforms the Jacobian as

$$T^{-1}JT = \begin{pmatrix} \rho & -\omega \\ \omega & \rho \end{pmatrix} \tag{A12}$$

where the eigenvalues of the Jacobian are $\lambda_\pm = \rho \pm i\omega$. We also have

$$\rho = -\frac{1}{2}\sqrt{\frac{E(\chi)}{S(\chi)}}[\mu + \alpha S'(\chi)] \tag{A13}$$

and

$$\omega^2 = -\rho^2 + \alpha\mu\, E'(\chi). \tag{A14}$$

The complex eigenvectors associated with $\lambda_\pm$ are

$$u_\pm = \begin{pmatrix} -\dfrac{\rho \pm i\omega}{2\alpha\sqrt{E(\chi)}} - \dfrac{\mu}{2\alpha\sqrt{S(\chi)}} \\ 1 \end{pmatrix}, \tag{A15}$$

and T is obtained from the real and imaginary parts of these complex eigenvectors, $u_r = \mathrm{Re}(u_+)$, $u_i = \mathrm{Im}(u_+)$:

$$T = (u_r\ u_i) = \begin{pmatrix} -\dfrac{1}{2\alpha}\left(\dfrac{\mu}{\sqrt{S(\chi)}} + \dfrac{\rho}{\sqrt{E(\chi)}}\right) & -\dfrac{1}{2\alpha}\dfrac{\omega}{\sqrt{E(\chi)}} \\ 1 & 0 \end{pmatrix}$$

and

$$T^{-1} = \begin{pmatrix} 0 & 1 \\ -2\alpha\dfrac{\sqrt{E(\chi)}}{\omega} & -\dfrac{\rho}{\omega} - \dfrac{\mu}{\omega}\sqrt{\dfrac{E(\chi)}{S(\chi)}} \end{pmatrix}. \tag{A16}$$

The condition $\rho = 0$ determines the Hopf bifurcation, and at this point the transformations T and T^{-1} reduce to

$$T = \begin{pmatrix} \dfrac{S'(\chi)}{2\sqrt{S(\chi)}} & -\dfrac{1}{2}\sqrt{-\dfrac{S'(\chi)E'(\chi)}{E(\chi)}} \\ 1 & 0 \end{pmatrix} \tag{A17}$$

and

$$T^{-1} = \begin{pmatrix} 0 & 1 \\ 2\sqrt{-\dfrac{E(\chi)}{S'(\chi)E'(\chi)}} & -\sqrt{-\dfrac{S'(\chi)E(\chi)}{S(\chi)E'(\chi)}} \end{pmatrix}. \tag{A18}$$

Next, we implement the linear change of variables

$$\begin{pmatrix} x \\ y \end{pmatrix} = T^{-1}\begin{pmatrix} \sigma - \sigma_0 \\ \chi - \chi_0 \end{pmatrix}, \tag{A19}$$

which leads to the system of ODE's

$$\begin{pmatrix} \dot{x} \\ \dot{y} \end{pmatrix} = \begin{pmatrix} \rho & -\omega \\ \omega & \rho \end{pmatrix}\begin{pmatrix} x \\ y \end{pmatrix} + \begin{pmatrix} f(x,y) \\ g(x,y) \end{pmatrix}. \tag{A20}$$

The stability coefficient a determines whether the bifurcation is super- or subcritical. In normal form, this coefficient can be directly obtained from the derivatives of the functions f and g:

$$a = \frac{1}{16}(f_{xxx} + f_{xyy} + g_{xxy} + g_{yyy}) + \frac{1}{16\omega}[f_{xy}(f_{xx} + f_{yy}) - g_{xy}(g_{xx} + g_{yy}) - f_{xx}g_{xx} + f_{yy}g_{yy}].$$

We then obtain, at the Hopf bifurcation point,

$$f_{xx} = \frac{\alpha\sqrt{E(\chi)}[S'(\chi)^2 - 2S(\chi)S''(\chi)]}{2S(\chi)^{3/2}},$$

$$f_{xy} = \frac{\alpha\sqrt{-S'(\chi)}E'(\chi)}{2E(\chi)},$$

$$f_{yy} = -\frac{\alpha S'(\chi)E'(\chi)}{2\sqrt{S(\chi)}\sqrt{E(\chi)}},$$

$$g_{xx} = \frac{\alpha\sqrt{-S'(\chi)}[E'(\chi)^2 - 2E(\chi)E''(\chi)]}{2E(\chi)\sqrt{E'(\chi)}},$$

$$g_{xy} = -\frac{\alpha\sqrt{E(\chi)}S'(\chi)^2}{S(\chi)^{3/2}},$$

$$g_{yy} = \frac{\alpha S'(\chi)\sqrt{-S'(\chi)}\sqrt{E'(\chi)}}{2S(\chi)},$$

$$f_{xxx} = -\frac{3\alpha\sqrt{E(\chi)}S'(\chi)}{4\sqrt{S(\chi)}}\left(\frac{S'(\chi)}{S(\chi)} - \frac{E'(\chi)}{E(\chi)}\right) \times\left(\frac{S'(\chi)}{S(\chi)} - 2\frac{S''(\chi)}{S(\chi)}\right) - \frac{\alpha\sqrt{E(\chi)}S^{(3)}(\chi)}{\sqrt{S(\chi)}},$$

$$f_{xyy} = \frac{\alpha S'(\chi)E'(\chi)[E(\chi)S'(\chi) - S(\chi)E'(\chi)]}{4S(\chi)^{3/2}E(\chi)^{3/2}},$$

$$g_{yyy} = 0,$$

$$g_{xxy} = \frac{\alpha S'(\chi)^2[E(\chi)S'(\chi) - S(\chi)E'(\chi)]}{2S(\chi)^{5/2}\sqrt{E(\chi)}},$$

whence

$$a = \frac{\alpha\sqrt{E(\chi)}S''(\chi)}{32S(\chi)^{1/2}}\left(3\frac{S'(\chi)}{S(\chi)} - 3\frac{E'(\chi)}{E(\chi)} + 2\frac{E''(\chi)}{E'(\chi)} - 2\frac{S^{(3)}(\chi)}{S''(\chi)}\right).$$

We thus obtain a quite simple condition for the vanishing of a, which determines the points where the super- or subcritical character of the Hopf bifurcation changes:

$$\frac{S^{(3)}(\chi)}{S''(\chi)} = \frac{1}{2}\left(\frac{3S'(\chi)}{S(\chi)} - \frac{3E'(\chi)}{E(\chi)} + \frac{2E''(\chi)}{E'(\chi)}\right). \quad \text{(A21)}$$

With the specific functions E and S of our current interest, the parameter a reads

$$a = \frac{1}{16\chi^6}\exp\left[-\frac{\kappa}{\chi}\right]E_1(1-\kappa)(\kappa - 1 - 2\kappa\chi + 2\chi^2), \quad \text{(A22)}$$

which admits a single positive zero for $\kappa < 1$:

$$\chi_{\text{crit}} = \frac{1}{2}(\kappa + \sqrt{2 - 2\kappa + \kappa^2}). \quad \text{(A23)}$$

This value defines a critical value for the parameter μ at the Hopf bifurcation,

$$\mu_{\text{crit}} = \frac{E_1}{E_0}\frac{1-\kappa}{\chi_{\text{crit}}^2}\exp\left[\frac{1-\kappa}{\chi_{\text{crit}}}\right] = \frac{E_1}{E_0}\frac{e^{-\kappa+\sqrt{2-2\kappa+\kappa^2}}}{1-\kappa}(\kappa - \sqrt{2-2\kappa+\kappa^2})^2,$$

and the critical strain rate

$$\dot{\epsilon}_{\text{crit}} = \sqrt{\frac{E_1E_0}{\alpha}}\exp\left[-\frac{\kappa+1}{\kappa-1}(\kappa - \sqrt{2-2\kappa+\kappa^2})\right].$$

[1] R. G. Horn and J. N. Israelachvili, J. Chem. Phys. **75**, 1400 (1981).
[2] H. K. Christenson, D. W. R. Gruen, R. G. Horn, and J. N. Israelachvili, J. Chem. Phys. **1834**, 1400 (1987).
[3] J. N. Israelachvili, P. M. McGuiggan, and A. M. Homola, Science **240**, 189 (1988).
[4] M. Schoen, C. L. Rhykerd, D. J. Diesler, and J. H. Cushman, Science **245**, 1223 (1989).
[5] M. L. Gee, P. M. McGuiggan, J. N. Israelachvili, and A. M. Homola, J. Chem. Phys. **93**, 1895 (1990).
[6] P. A. Thompson and M. O. Robbins, Phys. Rev. A **41**, 6830 (1990).
[7] P. A. Thompson and M. O. Robbins, Science **250**, 792 (1990).
[8] S. Grannick, Science **253**, 1374 (1991).
[9] M. W. Ribarsky and U. Landman, J. Chem. Phys. **97**, 1937 (1992).
[10] P. A. Thompson, G. S. Grest, and M. O. Robbins, Phys. Rev. Lett. **68**, 3448 (1992).
[11] I. A. Bitsanis and C. Pan, J. Chem. Phys. **99**, 5520 (1993).
[12] B. N. J. Persson, Phys. Rev. Lett. **71**, 1212 (1993).
[13] M. J. Stevens and M. O. Robbins, Phys. Rev. E **48**, 3778 (1993).
[14] H. Yoshizawa, P. McGuiggan, and J. Israelachvili, Science **259**, 1305 (1993).
[15] H. Yoshizawa and J. Israelachvili, J. Phys. Chem. **97**, 11 300 (1993).
[16] G. Reiter *et al.*, J. Chem. Phys. **101**, 2606 (1994).
[17] B. N. J. Persson, Phys. Rev. B **50**, 4771 (1994).
[18] Y. B. Mel'nichenko, J. Schüller, R. Richert, and B. Ewen, J. Chem. Phys. **103**, 2016 (1995).
[19] M. Urbakh, L. Daikhin, and J. Klafter, Phys. Rev. E **51**, 2137 (1995).
[20] J. M. Carlson and A. A. Batista, Phys. Rev. E **53**, 4153 (1996).
[21] J. Gao, W. D. Luedtke, and U. Landman, J. Chem. Phys. **106**, 4309 (1996).
[22] A. L. Demirel and S. Granick, Phys. Rev. Lett. **77**, 2261 (1996).
[23] M. G. Rozman, M. Urbakh, and J. Klafter, Phys. Rev. E **54**, 6485 (1996).
[24] J. Gao, W. D. Luedtke, and U. Landman, Phys. Rev. Lett. **79**, 705 (1997).
[25] G. Luengo, F.-J. Schmitt, R. Hill, and Jacob Israelachvili, Macromolecules **30**, 2482 (1997).
[26] M. G. Rozman, M. Urbakh, J. Klafter, and F.-J. Elmer, J. Phys. Chem. B **102**, 7924 (1998).
[27] A. A. Batista and J. M. Carlson, Phys. Rev. E **57**, 4986 (1998).
[28] B. N. J. Persson, in *Sliding Friction: Physical Principles and Applications* (Springer-Verlag, Berlin, 2000).
[29] C. Drummond and J. Israelachvili, Macromolecules **33**, 4910 (2000).
[30] J.-L. Barrat and L. Berthier, Phys. Rev. E **63**, 012503 (2001).
[31] C. Drummond and J. Israelachvili, Phys. Rev. E **63**, 041506 (2001).
[32] L. Berthier and J.-L. Barrat, Phys. Rev. Lett. **89**, 095702 (2002).
[33] D. Gourdon and J. N. Israelachvili, Phys. Rev. E **68**, 021602 (2003).
[34] M. Robbins, e-print cond-mat/0303276.
[35] T. Baumberger, P. Berthoud, and C. Caroli, Phys. Rev. B **60**, 3928 (1999).
[36] L. Bureau, T. Baumberger, and C. Caroli, Eur. Phys. J. E **8**, 331 (2002).
[37] A. Lemaître, Phys. Rev. Lett. **89**, 195503 (2002).
[38] A. Lemaître, e-print cond-mat/0206417.
[39] J. Gao, W. D. Luedtke, and U. Landman, Tribol. Lett. **9**, 3 (2000).
[40] B. N. J. Persson, Phys. Rev. B **48**, 18140 (1993).
[41] J. H. Dieterich, Pure Appl. Geophys. **116**, 790 (1978).

[42] J. H. Dieterich, J. Geophys. Res. B **84**, 2161 (1979).
[43] A. Ruina, J. Geophys. Res. B **88**, 10359 (1983).
[44] J. H. Dieterich and B. D. Kilgore, Pure Appl. Geophys. **143**, 283 (1994).
[45] J. Rice and A. Ruina, J. Appl. Mech. **105**, 343 (1983).
[46] J. R. Rice and S. T. Tse, J. Geophys. Res., [Solid Earth Planets] **91**, 521 (1986).
[47] T. Baumberger, F. Heslot, and B. Perrin, Nature (London) **367**, 544 (1994).
[48] F. Heslot *et al.*, Phys. Rev. E **49**, 4973 (1994).
[49] T. Baumberger, C. Caroli, B. Perrin, and O. Ronsin, Phys. Rev. E **51**, 4005 (1995).
[50] L. C. E. Struik, *Physical Aging in Amorphous Polymers and Other Materials* (Elsevier, Houston, 1976).
[51] S. Nasuno, A. Kudrolli, and J. P. Gollub, Phys. Rev. Lett. **79**, 949 (1997).
[52] S. Nasuno, A. Kudrolli, A. Bak, and J. P. Gollub, Phys. Rev. E **58**, 2161 (1998).
[53] J.-C. Géminard, W. Losert, and J. P. Gollub, Phys. Rev. E **59**, 5881 (1999).
[54] W. Losert, J.-C. Géminard, S. Nasuno, and J. P. Gollub, Phys. Rev. E **61**, 4060 (2000).
[55] D. Gourdon (private communication).
[56] A. L. Demirel and S. Granick, Phys. Rev. Lett. **77**, 4330 (1996).
[57] A. Lemaître, cond-mat/0307216.
[58] M. L. Falk and J. S. Langer, Phys. Rev. E **57**, 7192 (1998).
[59] M. L. Falk and J. S. Langer, MRS Bull. **25**, 40 (2000).
[60] M. L. Falk, Phys. Rev. B **60**, 7062 (1999).
[61] F. Spaepen, Acta Metall. **25**, 407 (1977).
[62] A. Argon, Acta Metall. **27**, 47 (1979).
[63] A. Argon and H. Kuo, Mater. Sci. Eng. **39**, 101 (1979).
[64] F. Spaepen and A. Taub, in *Physics of Defects*, Les Houches Lectures, Session XXXV, edited by J.-P. Balian and M. Kleman (North-Holland Amsterdam, 1981), p. 133.
[65] A. Argon and L. Shi, Acta Metall. **31**, 499 (1983).
[66] A. K. Doolittle, J. Appl. Phys. **22**, 1471 (1951).
[67] A. K. Doolittle and D. B. Doolittle, J. Appl. Phys. **28**, 901 (1957).
[68] D. Turnbull and M. H. Cohen, J. Chem. Phys. **34**, 120 (1961).
[69] D. Turnbull and M. H. Cohen, J. Chem. Phys. **52**, 3038 (1970).
[70] G. S. Grest and M. H. Cohen, Adv. Chem. Phys. **48**, 455 (1981).
[71] E. R. Nowak *et al.*, Phys. Rev. E **57**, 1971 (1998).
[72] T. Boutreux and P. G. de Gennes, Physica A **244**, 59 (1997).
[73] R. Stinchcombe and M. Depken, Phys. Rev. Lett. **88**, 125701 (2002).
[74] P. A. Thompson and G. S. Grest, Phys. Rev. Lett. **67**, 1751 (1991).
[75] T. Becker, in *Geocomplexity and the Physics of Earthquakes*, Geophysical Monographs, Vol. 120, edited by J. Rundle, D. Turcotte, and W. Klein (AGU, Washington, DC, 2000).
[76] A. Mehta and S. F. Edwards, Physica A **157**, 1091 (1989).
[77] S. F. Edwards and R. B. S. Oakeshott, Physica A **157**, 1080 (1989).
[78] S. Edwards, in *Granular Matter: An Interdisciplinary Approach*, edited by A. Mehta (Springer-Verlag, New York, 1994), pp. 121–140.
[79] L. F. Cugliandolo and J. Kurchan, Prog. Theor. Phys. Suppl. **126**, 407 (1997).
[80] L. F. Cugliandolo, J. Kurchan, and L. Peliti, Phys. Rev. E **55**, 3898 (1997).
[81] I. K. Ono *et al.*, Phys. Rev. Lett. **89**, 095703 (2002).
[82] H. A. Makse and J. Kurchan, Nature (London) **415**, 614 (2002).
[83] K. Maeda and S. Takeuchi, Phys. Status Solidi A **49**, 685 (1978).
[84] K. Maeda and S. Takeuchi, Philos. Mag. A **44**, 643 (1981).
[85] S. Takeuchi and K. Maeda, Key Eng. Mater. **13–15**, 749 (1987).
[86] H. Eyring, J. Chem. Phys. **4**, 283 (1936).
[87] F. Bowden and D. Tabor, *The Friction and Lubrication of Solids I* (Clarendon Press, Oxford, 1950).
[88] V. Arnold, *Mathematical Methods of Classical Mechanics*, Graduate Texts in Mathematics Vol. 60 (Springer-Verlag, Berlin, 1974).